Mathematical Biosciences and Engineering

http://www.aimspress.com/journal/mbe

MBE, 23(1): 1–21.
DOI: 10.3934/mbe.2026001
Received: 11 July 2025
Revised: 06 October 2025
Accepted: 20 October 2025
Published: 20 November 2025

Research article

A general multi-stratum model for a nanofunctionalized releasing capsule: An experiment-driven computational study

Elia Onofri[1,*], Emiliano Cristiani[1], Andrea Martelli[2], Piergiorgio Gentile[3,4], Joel Girón Hernández[3,4,5] and Giuseppe Pontrelli[1]

[1] Istituto per le Applicazioni del Calcolo (IAC), National Research Council of Italy (CNR), Rome, Italy

[2] Dipartmento di Ingegneria E. Ferrari, Università di Modena e Reggio Emilia, Modena, Italy

[3] Centre for Biomaterials and Tissue Engineering, Universitat Politècnica de València, València, Spain

[4] Biomedical Research Networking Centre on Bioengineering, Biomaterials and Nanomedicine (CIBER-BBN), Carlos III Health Institute, 46022 Valencia, Spain

[5] Northumbria University, Applied Sciences Department, Newcastle upon Tyne, UK

* **Correspondence:** Email: elia.onofri@cnr.it.

Abstract: Releasing capsules are widely employed in biomedical applications as smart carriers of therapeutic agents, including drugs and bioactive compounds. Such delivery vehicles typically consist of a loaded core, enclosed by one or multiple concentric coating strata. In this work, we extended existing mechanistic models to account for such multi-strata structures, including possible concurrent erosion of the capsule itself, and we characterized the release kinetics of the active substance into the surrounding medium. We presented a computational study of drug release from a spherical microcapsule, modeled through a non-linear diffusion equation incorporating radial asymmetric diffusion and space- and time-discontinuous coefficients, as suggested by the experimental data specifically collected for this study. The problem was solved numerically using a finite volume scheme on a grid with adaptive spatial and temporal resolution. Analytical expressions for concentration and cumulative release were derived for all strata, enabling the exploration of parameter sensitivity—such as coating permeability and internal diffusivity—on the overall release profile. The resulting release curves provide mechanistic insight into the transport processes and offer design criteria for achieving controlled release. Model predictions were benchmarked against *in vitro* experimental data obtained under physiologically relevant conditions, showing good agreement and validating the key features of the model. The proposed model thus serves as a practical tool for predicting the behavior of composite coated particles, supporting performance evaluation and the rational design of next-generation drug delivery systems with reduced experimental effort.

Keywords: drug release; biocompounds; microcapsules; diffusion equations; numerical solution

1. Introduction

Polymeric microparticles (MPs) are receiving increasing interest as drug delivery systems [1, 2]. They present interesting features, such as different administration routes, and can encapsulate various bioactive molecules, including antibiotics, chemotherapeutics, and nutraceuticals [3–6]. Particularly, nutraceutical components are credited with a number of health benefits and are associated with market-driven research and product innovation, thus enhancing the quality and safety in the food and health sectors. However, during production, storage, and even during digestion, these products may be degraded prior to exerting a beneficial effect. Also, they are often sensitive to light, oxygen, and temperature, thus decreasing their shelf life. In addition, many nutraceuticals are sensitive to the digestive environment and processes, which can affect their bioactivity. Therefore, understanding the transit, absorption, and bioavailability through the gastrointestinal tract is a keystone for designing tailored releasing MPs for nutraceuticals [6].

A possible approach to enhance nutraceuticals' survivability is given by encapsulation, which preserves and protects them through digestion until they reach the absorption region, where MPs should break down and release their content. Currently, smart versatile particles, based on stimuli-responsive materials capable of responding to the biochemical alterations of the environment, such as pH, have attracted great interest due to their structural and morphological advantages. Furthermore, the release of the MP payload can be easily tuned by selecting a suitable polymer and its chemical characteristics, such as monomer composition and molecular weight [7]. Another important aspect is the selection of the manufacturing method, according to the drug and specific applications, by which active molecules can be released at a programmed rate to the site of pharmacological action [8, 9].

A matrix platform, where an active agent is uniformly dispersed, is sometimes used. However, multi-stratum coated systems are nowadays more commonly employed. These MPs are constituted by a drug-loaded spherical core, surrounded by one or few polymeric concentric strata (shells) [10]. In a typical microcapsule (MC), the core has a size of hundreds of micrometres, and the multi-stratum enveloping structure can vary from hundreds of nanometres to a few micrometres. Such multi-stratum encapsulation enhances the structural stability and biocompatibility, allows the storage of different active agents, and protects the therapeutic agents from external chemical aggression, mechanical erosion, and premature degradation [8].

Different technologies have emerged in the last years to design and build multi-stratum MCs [11–13]. Various biomacromolecules—such as proteins, carbohydrates, and their combinations—have been explored for nutraceutical ingredients' protection and stability [14]. Polysaccharides like alginate, chitosan, starch, and carboxymethyl cellulose offer strong film-forming and chemical stability, improving resistance under harsh conditions [15]. In particular, alginate is a polysaccharide composed of β-D-mannuronic acid (M) and α-L-guluronic acid (G) residues arranged in varying sequences. It forms hydrogels in the presence of divalent cations such as $Ca^{2,+}$ through ionic cross-linking, particularly with G-blocks. Also, alginate is biocompatible, biodegradable, and readily degrades in the intestines, making it suitable for biomedical and food applications [16].

While classical *in vitro* and *in vivo* experimental techniques remain essential, mathematical and computational modeling offers an alternative tool in drug delivery design and provides more insights on the effects of various geometrical and physical conditions that can be useful to drastically reduce the number of experiments and, also, to provide a better design and manufacturing of drug-

loaded systems [17]. To this aim, fully mechanistic continuum models are commonly used, being based on physics-based equations that account for parameters having a direct physico-chemical meaning [10, 11]. In this context, we develop a continuum-scale mathematical model to evaluate the transport and release of combined drug and nutraceutical components from spherical shell-coated MPs immersed in a fluid environment with time-varying pH. In particular, the model accounts for several different components (core and coating by multiple strata of arbitrary thickness) and considers (i) the incorporation of nutraceutical components into the core and (ii) the diffusion and retention of a therapeutic agent from a polymeric MC.

Although diffusion equations have been extensively studied in the literature [18], the size contrast between the core and the shell strata of the MC, as well as the progressive erosion the capsule undergoes, pose interesting numerical challenges worth investigating. To obtain meaningful results, we employ a finite volume scheme with variable space and time steps, together with a careful treatment of the interfaces between strata, to be interpreted as internal boundary conditions. All numerical simulations presented in this work were carried out with a custom-made MATLAB code specifically developed for this study, ensuring full control over the algorithmic implementation and flexibility in exploring different model configurations*. Furthermore, experimental data specifically collected for this study suggested the inclusion of radial asymmetric diffusion in the mathematical model, namely a directional dependence of the effective diffusivity for inward versus outward flux. This feature proved particularly useful to reproduce the release kinetics in the first (internal) strata, often characterized by the distinct behavior of the pre-coating.

After a preliminary study of the multi-strata impact on the numerical model, we proceed by identifying the relevant parameters over a set of *in vitro* experiments, and we perform a sensitivity analysis to understand the influence of different model conditions and configurations on the release behavior. We show that the model is capable of fitting the observed experimental data and, thus, can be used as a predictive tool. The results of our model show good agreement with the data reported in the literature and with the carried-out experiments.

2. The proposed model

Let us consider a multi-stratum spherical microcapsule (MC) made of a core (the depot, Ω_1) surrounded by a sequence of $L-1$ concentric polymeric coating strata (Ω_ℓ, with $\ell = 2, ..., L$), as illustrated in Figure 1. The core is typically larger in size (hundreds of micrometres) and contains the principal compound like, e.g., drugs or nutraceuticals. Conversely, the enveloping strata have limited thickness (hundreds of nanometres) and are constituted of different, yet homogeneous and isotropic, materials, which increase capsule resistance and structural stability. In the case of a releasing MC, such strata might be filled with various auxiliary compounds at different concentrations and can be customized to allow selective diffusion, to better control the release rate [8]. The size of these strata may vary considerably from one another, up to some micrometres. An outer thin protective film, which is generally considered as a membrane, is also included. This membrane shields and preserves the encapsulated compounds from degradation and fluid convection, protects the MC overall structure, and guarantees a more controlled and sustained release [10]. However, upon ingestion, the membrane immediately dissolves and the outer stratum Ω_L is considered in contact with the targeted release medium (either

*https://github.com/eOnofri04/NRMc.

a bulk fluid or tissue). During the transit in the digestive tract, the external shells are exposed to the unfavorable and aggressive environment of variable pH and undergo a progressive erosive process. The biocompound transport within the MC is driven by pure diffusion, but predicting kinetics is not an easy task, due to the multi-stratum structure and the domains' thickness contrast.

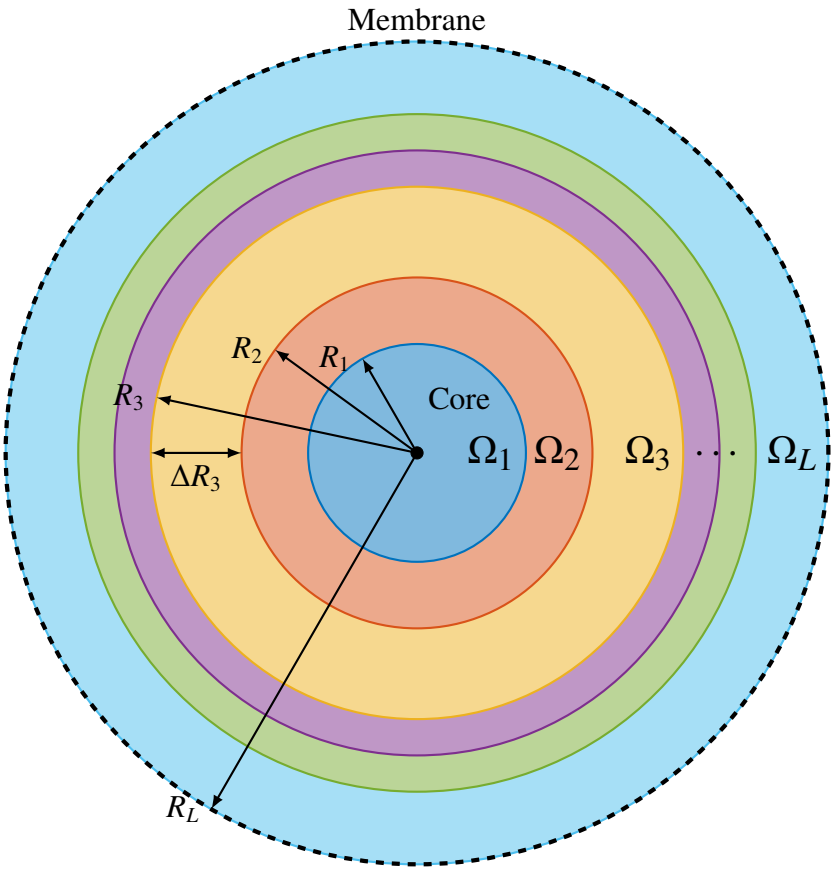

Figure 1. Cross-section of the multi-stratum MC. Figure not to scale.

Furthermore, experiments show that, due to electrostatic interactions with long polymeric chains, a low percentage of travelling molecules remain entrapped and are retained within the polymeric multi-strata without any release. We model this aspect by assuming that, while diffusing, part of the drug through the coating can potentially be permanently bound at a given rate [12]. In other cases, a natural decay of the drug can occur.

2.1. The general formulation

Let us consider a general structure made of $L-1$ strata $\Omega_2, \ldots, \Omega_L$ surrounding a core Ω_1, hence forming, as a whole, a capsule with a protective shell. Each domain individually, or a group of domains, is filled with S diffusing substances—typically, different substances are initially deployed in the core and the strata, yet they can move freely upon ingestion. Let us denote by $c^s(x,t)$ the concentration of the substance (or phase) s at point x and time t. Note that the position x univocally identifies either a capsule's stratum Ω_ℓ, $\ell = 2, \ldots, L$, or the core Ω_1.

In the following multi-stratum general model, the biocompound transport in each domain Ω_ℓ, $\ell =$

$1, \dots, L$, can be described by the second Fick's diffusion law and the decay/binding processes as first-order reaction kinetics:

$$\frac{\partial c^s}{\partial t} = \nabla \cdot (D_\ell^s \nabla c^s) - \beta_\ell^s c^s \qquad \text{in } \Omega_\ell\,, \quad s = 1, \dots, S\,, \tag{2.1}$$

where D_ℓ^s is the diffusion coefficient and β_ℓ^s represents the reaction rate of the s-th phase in the ℓ-th domain Ω_ℓ. The initial concentrations

$$c^s(\cdot, 0) = c_0^s(\cdot) \qquad \text{in } \Omega_\ell\,, \quad s = 1, \dots, S\,, \tag{2.2}$$

are given in each domain, for all substances.

Contiguous domains are paired by imposing density and flux continuity at the interface, namely, for all times t:

$$c^s(x^-, t) = c^s(x^+, t) \qquad \text{at } x \in \Omega_{\ell-1} \cap \partial\Omega_\ell\,, \qquad \ell = 2, \dots, L\,, \tag{2.3}$$

$$-D_{\ell-1}^s \nabla c^s(x^-, t) \cdot \hat{n} = -D_\ell^s \nabla c^s(x^+, t) \cdot \hat{n} \qquad \text{at } x \in \Omega_{\ell-1} \cap \partial\Omega_\ell\,, \qquad \ell = 2, \dots, L\,, \tag{2.4}$$

where $\hat{n}$ is the surface external normal unit vector and $x^\pm$ denotes the inner/outer limit as usual. Finally, the Robin boundary condition is used on the outer stratum, i.e.,

$$-D_L^s \nabla c^s \cdot \hat{n} = \lambda^s c^s \qquad \text{at } \|x\| = R_L\,, \tag{2.5}$$

where $\lambda^s \geq 0$ (ms^{-1}) is a mass transfer coefficient for substance s, expressing the surface coating finite resistance. As a special case, $\lambda^s = 0$ (resp., $\lambda^s \to \infty$) represents an impermeable (resp., perfect sink) boundary.

2.2. The radial symmetric equations

In the above configuration, we assume each stratum has the shape of a concentric spherical shell (annulus) of increasing radius. Due to the homogeneity, we can assume that net drug diffusion occurs along the radial direction only, and thus we restrict our study to a one-dimensional model for the function $c^s(r, t)$, where r represents the radial coordinate. Here we denote by R_ℓ and $\Delta R_\ell := R_\ell - R_{\ell-1}$, respectively, the radius and the thickness of Ω_ℓ (cf. Figure 1), where we assume $R_0 = 0$. Thus, the general formulation given in the previous section reduces to a system of $L \times S$ equations, which in 1D radial symmetry reads, for any $\ell = 1, \dots, L$ and $s = 1, \dots, S$, as

$$\frac{\partial c^s}{\partial t} = \frac{1}{r^2}\frac{\partial}{\partial r}\left(D_\ell^s \left(\frac{\partial c^s}{\partial r}\right) r^2 \frac{\partial c^s}{\partial r}\right) - \beta_\ell^s c^s\,, \qquad r \in (R_{\ell-1}, R_\ell)\,, \tag{2.6}$$

$$c^s(r, 0) = c_0^s(r)\,, \qquad r \in (R_{\ell-1}, R_\ell)\,, \tag{2.7}$$

$$\frac{\partial c^s}{\partial r} = 0\,, \qquad r = 0\,, \tag{2.8}$$

$$-D_{\ell-1}^s \frac{\partial c^s(r^-, t)}{\partial r} = -D_\ell^s \frac{\partial c^s(r^+, t)}{\partial r}\,, \qquad r = R_{\ell-1}\,, \tag{2.9}$$

$$-D_L^s \frac{\partial c^s}{\partial r} = \lambda^s c^s\,, \qquad r = R_L\,, \tag{2.10}$$

where c_0^s is the initial concentration defined in Eq 2.2. Note that in Eq 2.6 we have included the dependence of D on the derivative of c with respect to r, which makes the equation nonlinear. This was done to allow a possible radial asymmetric diffusion in the diffusion dynamics, meaning that, for a given r, the diffusion toward the center can be different from the diffusion toward the outer boundary [19]. In the following experiments, we simply define it as a piecewise constant value, depending on the flux direction only, i.e., for $\ell = 1, \dots, L$:

$$D_\ell^s\left(\frac{\partial c^s}{\partial r}\right) = \begin{cases} D_\ell^{s,+} & \text{if } \dfrac{\partial c^s}{\partial r} < 0 \\ D_\ell^{s,-} & \text{if } \dfrac{\partial c^s}{\partial r} \geq 0 \end{cases}, \tag{2.11}$$

where we define the inward diffusivity radial asymmetric factor $\alpha_\ell^s \geq 0$ as the ratio $\alpha_\ell^s := D_\ell^{s,-}/D_\ell^{s,+}$ (here α is an index denoting the degree of (inward) asymmetry in the radial diffusion, with $\alpha = 1$ being fully symmetric, $\alpha = 0$ admitting outward flux only, and $\alpha = +\infty$ admitting inward flux only). Figure 2 shows the 1D domain with the stratum division and how to manage the diffusion asymmetry.

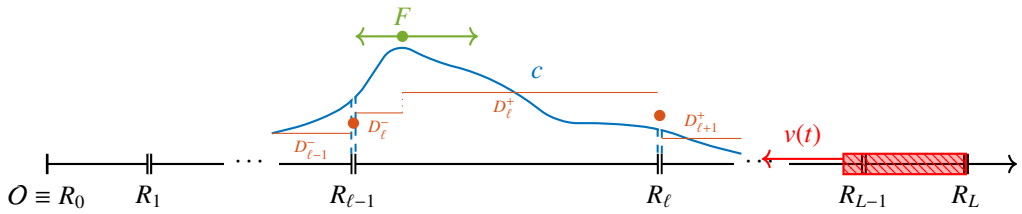

Figure 2. 1D radial domain with stratum division for a single substance. Diffusion coefficients depend both on the stratum and the direction of the mass flux F. The red zone on the far right denotes the inward erosion, see Section 2.3.

Computing the released mass To characterize the release process, we evaluate the cumulative mass m of the released compound s as a function of time. This quantity can be obtained by integrating the corresponding concentration fluxes over the outer surface of the MC. In formulas, we obtain

$$m^s(t) = \int_0^t \left(\int_{\partial\Omega_L} -D_L^s \nabla c^s \cdot \hat{n}\, d\Sigma \right) d\tau\,, \qquad s = 1, \dots, S\,, \tag{2.12}$$

which, under radial symmetry, reduces to

$$m^s(t) = -4\pi R_L^2 \int_0^t D_L^s \frac{\partial c^s(R_L, \tau)}{\partial r} d\tau\,, \qquad s = 1, \dots, S\,. \tag{2.13}$$

2.3. Modeling the erosion

So far, we have assumed the domain of the MC remains unchanged throughout the process. However, because of water imbibition and chemical interactions with the release medium, or due to the unfavorable pH of the environment, the MC undergoes a degradation/erosion process on its surface. As a consequence, the external stratum erodes and its radius reduces over time, progressively melting the strata until the core itself becomes exposed. At that point, the whole capsule, left without any protective shell, typically disintegrates.

From the modeling perspective, let $R(t)$ be the radius of the sphere at time t. The speed of erosion dR/dt can be modeled as some positive function $v_e(t)$ such that

$$R(t) := \max\left\{R_1, R_L - \int_0^t v_e(\tau)\, d\tau\right\}, \qquad t \geq 0. \tag{2.14}$$

The simulation domain shrinks progressively, and the domain for Eq 2.6 becomes $(R_{\ell-1}, \min\{R_\ell, R(t)\})$, see Figure 2. As a consequence, when $R(t) \leq R_{\ell-1}$, then Ω_ℓ is considered completely eroded and its contribution is removed from the model; hence, we denote with ℓ_L the most external non-eroded domain. Note that we will consider the function $v_e(t)$ as assigned or estimated from experiments.

Clearly, if Eq 2.6 is solved assuming a fixed domain at any time, then an additional term is required to take into account the mass instantaneously released due to volume erosion. Hence Eq 2.13 reads as:

$$m^s(t) = -4\pi \int_0^t D^s_{\ell_L} R(\tau)^2 \frac{\partial c^s\,(R(\tau),\tau)}{\partial r}\, d\tau + 4\pi \int_0^t c^s\,(R(\tau),\tau)\; R^2(\tau)\, v_e(\tau)\, d\tau\,, \tag{2.15}$$

where, for the additional term, we have considered that the infinitesimal mass element dm is given by the concentration c^s multiplied by the infinitesimal annulus volume element swept by R in time dt, $dV = \frac{4}{3}\pi((R+dR)^3 - R^3) \approx 4\pi R^2 dR$ (first-order approximation), and, finally, $dR = v_e dt$.

3. The numerical model

In this section, we detail the numerical method used for approximating the system Eqs 2.6–2.10. Due to strata thickness contrast (several orders of magnitude between the core and external strata), a numerical grid with variable space and time steps is required. Moreover, the erosion moves the MC surface inwards and requires attention to the right boundary condition.

Since the kinetics of concentrations are independent of one another, and all undergo similar evolution in space and time, in what follows, we will refer to a generic concentration c, omitting the s index.

3.1. The numerical scheme for a fixed domain

We preliminarily assume that we are dealing with a *time-independent* spherical domain, i.e., where $R(t) = \bar{R} = R_L$, $\forall t$. We assume $t_0 = 0$ as the initial time and $r = 0$ is the center of the *in silico* capsule. The numerical solution is found in the spatio-temporal domain $[0, \bar{R}] \times [0, T]$, by tracking the evolution of $c(r,t)$ and the corresponding released mass $m(t)$. For numerical convenience, we divide each stratum ℓ into a number of grid cells, say N_ℓ, of constant length Δr^ℓ. The center of the j-th cell of the ℓ-th stratum is denoted by r^ℓ_j and its value corresponds to the distance from the center of the capsule to the center of the cell itself. Following the same notation, we denote by $[r^\ell_{j-1/2}, r^\ell_{j+1/2})$ the j-th cell of the ℓ-th stratum, with $r^\ell_{j\pm 1/2} := r^\ell_j \pm \frac{\Delta r^\ell}{2}$. Finally, we denote by Δt the time step, and by n the index for counting the time steps, so $n\Delta t$ gives the current time.

The numerical solution will be given by the values $C^{\ell,n}_j$, for all ℓ, j, and n, which approximate the average concentration in each cell at each time step in each stratum [20],

$$C^{\ell,n}_j \approx \frac{1}{\Delta r^\ell} \int_{r^\ell_{j-1/2}}^{r^\ell_{j+1/2}} c(r, n\,\Delta t) dr. \tag{3.1}$$

We recall that, due to the spherical symmetry, the interfaces between cells are spherical shells of surface area

$$A_{j+1/2} = 4\pi r_{j+1/2}^2, \tag{3.2}$$

and that the j-th cell accounts for a total volume of

$$V_j = \frac{4}{3}\pi(r_{j+1/2}^3 - r_{j-1/2}^3). \tag{3.3}$$

The stratum-dependent diffusion coefficients can be discretized at interfaces using the harmonic mean,

$$\hat{D}_{j+1/2}^{\ell} := \begin{cases} D_\ell^+, & \text{if } C_j^\ell \geq C_{j+1}^\ell \text{ and } R_{\ell-1} \leq r_{j+1/2} < R_\ell, \\ D_\ell^-, & \text{if } C_j^\ell < C_{j+1}^\ell \text{ and } R_{\ell-1} \leq r_{j+1/2} < R_\ell, \\ \dfrac{2D_\ell^+ D_{\ell+1}^+}{D_\ell^+ + D_{\ell+1}^+}, & \text{if } C_j^\ell \geq C_{j+1}^\ell \text{ and } r_{i+1/2} = R_\ell, \\ \dfrac{2D_\ell^- D_{\ell+1}^-}{D_\ell^- + D_{\ell+1}^-}, & \text{if } C_j^\ell < C_{j+1}^\ell \text{ and } r_{i+1/2} = R_\ell. \end{cases} \tag{3.4}$$

From now on, when possible, we drop the index ℓ for readability. In Figure 3, we depict the numerical setting at the junction between a sample coarse and fine grid, and we visualize the quantity $\hat{D}$ defined at the interfaces.

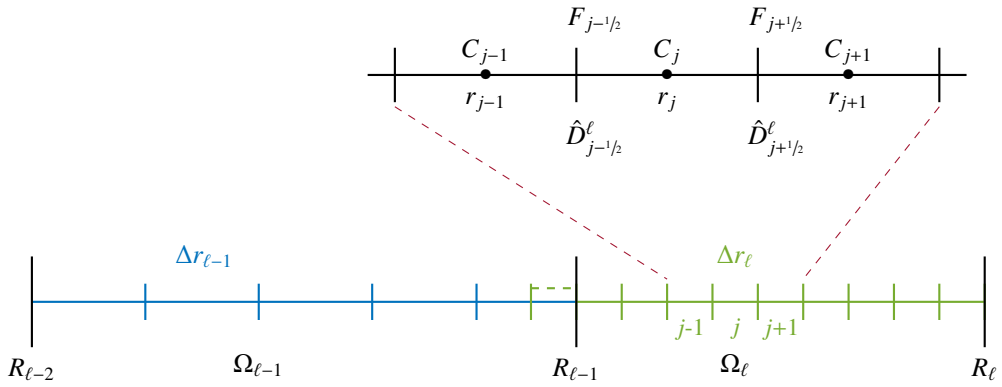

Figure 3. Grids and variable settings. Coarse grid on $\Omega_{\ell-1}$ and fine grid on Ω_ℓ. Inner cells zoom: diffusion coefficients $\hat{D}$ (Eq 3.4) and numerical fluxes F (Eq 3.5) are defined at the cell interfaces, diffusion coefficients D and concentrations C, instead, are defined at the cell centers. The dashed cell is the ghost cell for the fine grid.

Diffusion in spherical symmetry The second-order operator in Eq 2.6 can be approximated by means of the following finite volume discretization

$$\frac{1}{r^2}\frac{\partial}{\partial r}\left(D\, r^2 \frac{\partial c}{\partial r}\right)\bigg|_{r=r_j} \approx \frac{1}{r_j^2}\frac{1}{\Delta r}\left(\underbrace{\hat{D}_{j+1/2}\, r_{j+1/2}^2 \frac{C_{j+1}^n - C_j^n}{\Delta r}}_{F_{j+1/2}} - \underbrace{\hat{D}_{j-1/2}\, r_{j-1/2}^2 \frac{C_j^n - C_{j-1}^n}{\Delta r}}_{F_{j-1/2}}\right), \tag{3.5}$$

where $F_{j+1/2}$ and $F_{j-1/2}$ are the right-outward and left-inward numerical fluxes of the cell j, respectively (cf. Figure 3).

Time derivative For what concerns the time derivative $\frac{\partial c}{\partial t}$, a natural choice is forward finite differences,

$$\left.\frac{\partial c}{\partial t}\right|_{r=r_j} \approx \frac{C_j^{n+1} - C_j^n}{\Delta t}. \tag{3.6}$$

Complete scheme in each stratum Overall, the complete numerical scheme reads

$$C_j^{n+1} = C_j^n + \frac{\Delta t}{\Delta r\, r_i^2}(F_{j+1/2} - F_{j-1/2}) - \Delta t \beta_j C_j^n, \tag{3.7}$$

where the last term accounts for the decay process and it is considered fully independent of space and of the diffusion process. The above numerical scheme is stable only under the CFL condition [20]:

$$\Delta t \leq \frac{\Delta r^2}{2 \max_j(\hat{D}_{j\pm 1/2})}. \tag{3.8}$$

Stratum interfaces and variable space-time steps Some important remarks are in order:

- The big difference between the thickness of the core and that of the coating strata suggests using different space steps. To this end, it is convenient to assume that space steps Δr are constant in each stratum and are all multiples of the smallest one. This makes computation easier to manage. Moreover, when two strata with different space steps join together, we compute the mass balance at the interface only on the side of the finer grid. To do that, a ghost cell, with a size equal to the small cell, is placed on the side of the stratum with large cells (cf. Figure 3). The value of the concentration of the ghost cell is assumed to be equal to the value of the large cell in which it is embedded. Once the mass balance in the small cell is computed, it is used (with the opposite sign) for evaluating the mass balance in the large cell.
- The CFL condition [20] presented in Eq 3.8 must be kept as sharp as possible (ideally it should be satisfied with equality), in order to avoid numerical diffusion (for computational accuracy) and to avoid small time steps (for computational efficiency). Therefore, strata with different space steps must have different time steps, which means that not all strata are updated with the same frequency. Coming back to the mass balance at stratum interfaces discussed before, different time steps require storing in a buffer the mass which must pass from the fine to the coarse layer, in such a way that the right amount of mass is transferred when the coarse grid is eventually updated.
- The large difference between space steps introduces some unfeasible dynamics in the numerical approximation. For example, when some mass is transferred from the fine to the coarse grid, the mass spreads instantaneously along the whole large cell (since at each given time the concentration value is constant in each cell), thus covering a distance which is too large to be consistent with the physics of the problem. On the other side, when some mass is transferred from the coarse to the fine grid in one time step (the large one), the mass has enough time to travel through the entire neighboring small cell and reach the next small cell, but this is not allowed by the CFL condition, being a 3-point stencil used here (Figure 3). To overcome this problem, we introduce one or more domains (fictitious strata), which allows us to move *continuously* from the coarse to the fine grid (or vice-versa), thus avoiding excessive differences in the grid size. The model,

in fact, includes the possibility of having a large number of domains, not only to describe the experimental physical strata with due accuracy, but also for numerical reasons.

Boundary conditions at $r = \bar{R}$ At the outer boundary, the Robin condition (see Eq 2.5) is imposed by means of an additional ghost cell, indexed by $N_L + 1$, where we set

$$C^n_{N_L+1} = C^n_{N_L}\left(1 - \Delta r^L \lambda\right) , \tag{3.9}$$

corresponding to an outgoing flux (cf. Eq 3.5) through the last interface $N_L + 1/2$ given by

$$F_{N_L+1/2} = \hat{D}_{N_L+1/2}\, r^2_{N_L+1/2}\, \lambda C_{N_L} . \tag{3.10}$$

Modeling the erosion So far, we have discussed the problem by considering a fixed spatial domain. Now we generalize the model accounting for the erosion term, as defined in Eq 2.14. In order to keep the numerical implementation as simple as possible, we have assumed that the external boundary condition Eq 3.9 progressively moves inward. Moreover, we never allow a cell to be only partially eroded. Instead, we reduce the domain by one cell only when it is fully disintegrated. When this happens, all the mass contained in that cell is released, and the ghost cell accounting for the external boundary condition is shifted one cell inward.

4. Numerical validation

In this section, we introduce a few simple tests to prove the model effectiveness and to validate the numerical method. Let us consider a homogeneous sphere of $R = 100\,\mu$m, filled with a given substance with constant density of $c_0 = 1\ \mu\text{g}/\mu\text{m}^3$, and let us assume a diffusion coefficient $D = 0.01\ \mu\text{m}^2/\text{s}$. For the sake of simplicity, let us assume the substance being non-decaying ($\beta = 0\ \text{s}^{-1}$) and the MC is not eroding ($v = 0\ \mu$m/s) and isotropic ($\alpha = 1$). The total mass ($m = 4.188$ g) should then completely leave the medium (up to $\sim 99.9\%$) within 4 hours ($T = 14{,}400$ s). The parameters are summarized in Table 1.

Table 1. The set of parameters used in preliminary tests.

R [μm]	T [min]	c_0 [μg/μm^3]	D [μm^2/s]	β [s^{-1}]	v [μm/s]	λ [μm/s]	α [-]
100	240	1	0.5	0	0	1	1

In order to capture possible numerical differences between mono- and multi-stratum systems, we run the same physical model under a variety of different grid combinations:

One-stratum, extremely fine grid, reference case. We set a single extremely fine grid as a reference (exact) solution, setting $\Delta r = 0.01\ \mu$m and setting the corresponding time discretization to $\Delta t = 10^{-5}$ s, a reasonable value according to the CFL condition required for the stability of the scheme.

One-stratum, fine grid. We set a single fine grid as the best-case benchmark, setting $\Delta r = 0.1\ \mu$m and $\Delta t = 10^{-3}$ s.

One-stratum, coarse grid. We set a single coarse grid as a worst-case benchmark, setting $\Delta r = 1\ \mu$m and $\Delta t = 0.1$ s.

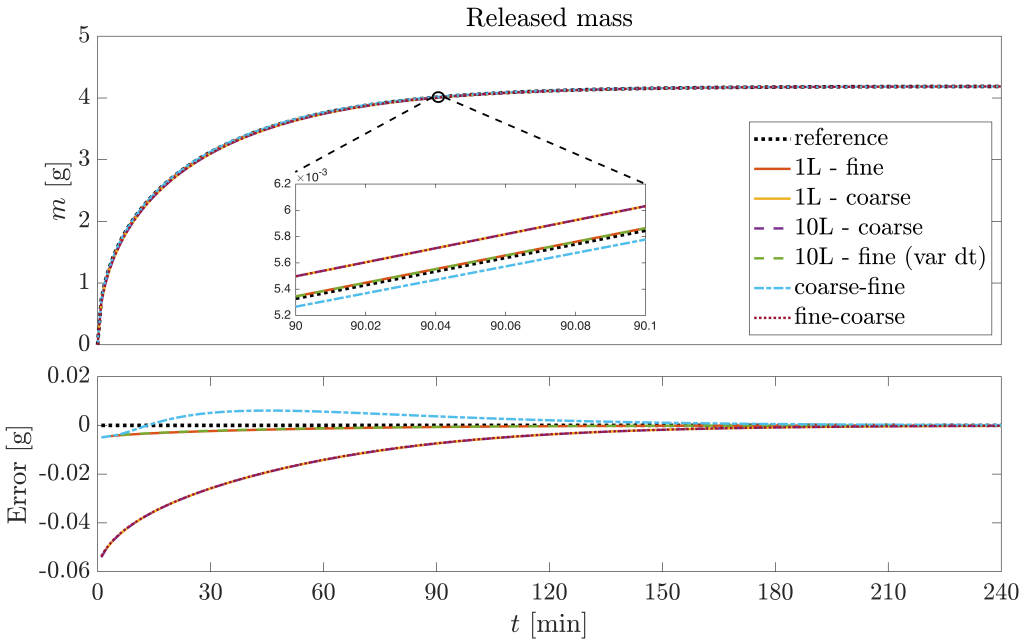

Figure 4. Released cumulative mass (top) and corresponding signed error (bottom) as a function of time, for the reference solution and the other 6 configurations.

10-strata, constant coarse grid. We run the simulation over 10 evenly spaced strata, employing the very same discretization as in the coarse grid example for each stratum, so as to verify the impact of the multi-grid over-engineering.

10-strata, variable-time fine grid. As before, we adopted 10 strata and we fixed the spatial discretization to the one of the fine grid, i.e., $\Delta r = 0.1$ μm; however, we set variable Δts, ranging between $5 \cdot 10^{-5}$ and 10^{-3} to understand the impact of different temporal discretization on the results. In particular, we set both progressive refinements and coarsening of Δt between strata as follows:

$$\Delta t = 10^{-3} \cdot [1, 0.5, 0.1, 0.05, 0.1, 0.5, 1, 0.05, 0.05, 1]$$

2-strata, coarse-fine coupled grid. We coupled the coarse grid and the fine grid by running the simulation over an internal stratum of 75 μm coarse-discretized and an external stratum of 25 μm fine-discretized.

2-strata, fine-coarse coupled grid. By reversing the previous configuration, we finally coupled an external coarse grid with an internal fine grid.

In Figure 4, we plot the release curve (top) and the absolute error (bottom, point-wise signed distance from the reference) for released mass computed every minute. Due to the absence of the binding effect, the whole initial mass is released within 240 minutes, as expected, which also explains why the error goes to zero in the limit, for each scenario. In Table 2, we report the corresponding discrepancies (vs. the reference mono-stratum finer grid approximation of the exact solution) along with the experiments summary. Figure 5 shows the concentration profiles along the radius at time intervals of 4 minutes. As expected, the concentration decays to zero after $\sim$ 4 h, with the release rate larger at early instants.

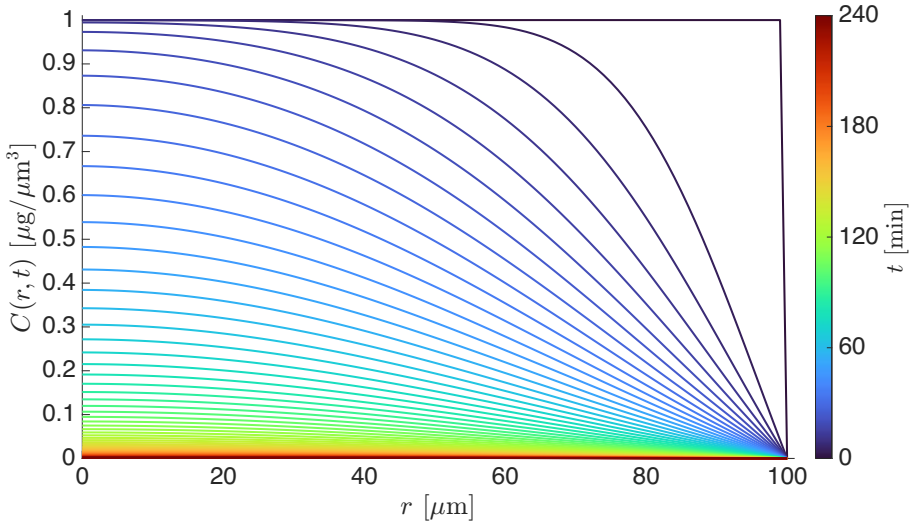

Figure 5. Concentration profiles at equidistant time intervals (240 s) along the radius. The color bar indicates the time scale.

Table 2. Relative error between the six different configurations compared with the reference case. In all cases, the error is relatively small.

Number of strata	**Grid**	Δr [μm]	Δt [s]	Mean relative error [%]
1	fine	0.1	0.001	0.034
1	coarse	1	0.1	0.376
10	coarse	1	0.1	0.376
10	fine (var Δt)	0.001	0.005–0.1	0.033
2	coarse+fine	1/0.1	0.02/0.001	0.073
2	fine+coarse	0.1/1	0.001/0.02	0.374

Unsurprisingly, the fine-grid solution minimizes discrepancy over the other experiments. However, the impact of the sole multi-stratum is negligible w.r.t. the single-stratum experiment (cf. coarse vs. coarse multigrid). Furthermore, the gain obtained from the improvement in Δt frequency in a multi-stratum environment actually overcomes the performance degradation introduced by the multiple strata themselves (cf. fine grid vs. multigrid fine). Finally, the disposition of the strata impacts the simulation accuracy, mainly depending on the flux direction (i.e., mass moving from coarse to fine or vice-versa).

5. A case study: The coated microcapsules

In this section, we first describe the experimental setup of the case study involving coated nano-engineered microcapsules, which serves as the basis for the numerical model introduced earlier. We then demonstrate the ability of the proposed model to reproduce the experimental data with good agreement. Finally, we present a sensitivity analysis to explore the influence of key model parameters.

5.1. Experimental setup

To ground our modeling approach in a realistic application, we consider a case study involving microcapsules nano-engineered via multi-strata coating. In what follows, we detail the experimental procedure adopted for the fabrication and characterization of the microcapsules, which provides both the physical context and quantitative data used to inform and validate our numerical model (statistics are presented as the average and standard deviation over 9 experimental repetitions).

For the core formation, alginate powder was dissolved in deionized water to prepare a 2 wt% solution. Then, the solution was transferred into a syringe and extruded through a 27 G conical tip into a 1% (w/v) $CaCl_2$ gelling solution. To achieve MC, an adapted electrospinning setup (Spinbox, Bioinicia, Spain) was employed. The process parameters included a flow rate of 500 μL/h, an applied voltage of 6.5 kV, and a 2-cm distance between the tip and the gelling bath. The MC diameter and circularity were evaluated using microscopy (Nikon Eclipse TS100), which revealed an average radius of 285 ± 18 μm and a circularity of 0.98 ± 0.02 (calculated from 2D optical images), see Figure 6A. Capsules were subsequently coated via coupled deposition of polysaccharides embedding the tannic acid (TA; Merck, UK) as the selected therapeutic agent. A Transmission Electron Microscopy (TEM, Philips CM 100 Compustage FEI) was used at a voltage of 100 kV for investigating the thickness of each stratum produced, revealing, with an instrumental resolution below 0.5 nm, an average value of 18 ± 1 nm.

During the initial deposition cycles, a couple of pre-coating strata typically forms, characterized by irregular adsorption and partial surface coverage. This early phase is crucial for modifying the surface chemistry and charge of the substrate, thereby improving its compatibility with the subsequent growth of ordered strata. As the deposition progresses, the pre-coating serves as an intermediate interface that promotes more uniform molecular organization, eventually leading to the formation of a continuous, homogeneous multi-strata film with well-defined thickness [21, 22]. This transition from a disordered or patchy initial stratum to an ordered stratified structure is particularly evident when working with low-reactivity or rough substrates.

Finally, the MCs were frozen at -80 °C and then freeze-dried for 24 h using an ALPHA 1–2 LD Plus freeze-dryer (Martin-Christ, Germany) for further analysis. No significant changes were observed in the size of the capsules after surface functionalization due to the nanometric thickness of the resulting shell, see Figure 6B.

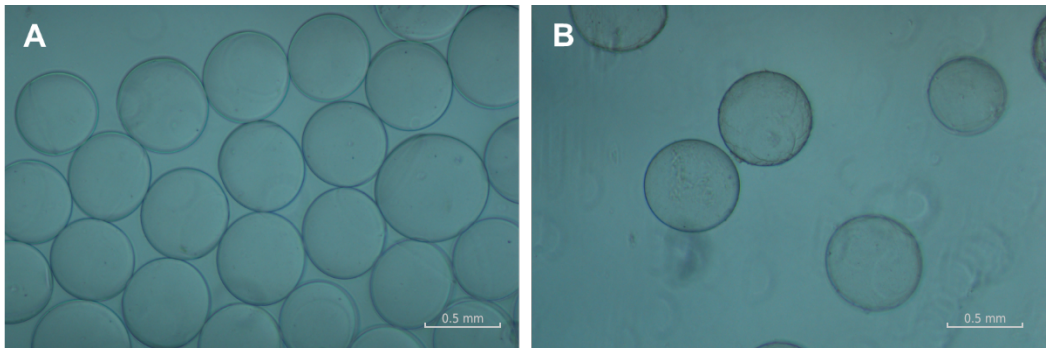

Figure 6. Optical images of MCs: (A) uncoated; (B) coated with the polysaccharide-based multi-strata shell, consisting of eight nanolayers with an average thickness of 18 ± 1 nm each. The coated MCs appear shaded, with darker borders.

To estimate the content of TA encapsulated within the shell, a dissolution test was conducted by immersing freeze-dried MCs in Phosphate-Buffered Saline solution (PBS, pH 7.4, 37 °C) for 48 hours to allow the degradation of the multi-stratum. The released TA solution was evaluated spectrophotometrically at 280 nm (FLUOstar Omega, BMG Labtech, Germany) and revealed a content of 4.721 ± 0.67 mg/mL in the coated MCs, corresponding to a mass of $m^{\mathrm{TA}} = 472.10 \pm 67\ \mu$g.

Then, *in vitro* digestion experiments were carried out according to the standardized INFOGEST 2.0 method, comprising sequential oral, gastric, and intestinal phases under physiologically relevant conditions [23]. In the oral phase, samples were mixed with simulated salivary fluid (SSF) containing α-amylase and incubated at 37 °C for 2 min. The gastric phase was performed using simulated gastric fluid (SGF) with pepsin (pH 3.0) and incubated at 37 °C for 2 h in a TSSWB15 shaking water bath (ThermoScientific, UK). The intestinal phase followed, using simulated intestinal fluid (SIF) containing pancreatin and bile salts (pH 7.0), also incubated at 37 °C for 2 h with constant shaking. Enzyme activities and electrolyte concentrations were adjusted according to INFOGEST guidelines.

Aliquots (50 μL) were withdrawn from the digestion mixtures at each phase (oral, gastric, and intestinal), specifically every 30 min during the gastric phase and every 15 min during the intestinal phase, to monitor the release of tannic acid from the beads (see also Figure 9). Negligible release was detected during the oral phase, indicating the multi-stratum coating effectively protected the core under salivary conditions. During the gastric phase, ~21.92% of the TA was released, likely due to partial disruption of the coating in the acidic environment. A more sustained release was observed in the intestinal phase, attributed to the combined effects of hydrolytic degradation and diffusion through the multi-stratum structure.

Concurrently with aliquot sampling, TEM nanometric measurements on the multi-stratum thickness were carried out to characterize the impact of the erosion process. Negligible erosion was detected (< 0.5%) during the oral phase, further confirming the coating effectiveness. Interestingly, extremely constrained erosion, corresponding to 3.24% of the total thickness, was measured during the gastric phase, prompting the release of the TA being ascribable to diffusive processes mainly. Conversely, the consistent erosion during the intestinal phase positively correlates with the higher measured TA releases, suggesting it as the main contributor in the release process. Also noteworthy is the sudden change within erosion speed upon reaching the last two strata, see Figure 7, further suggesting a structural difference between the pre-coating and the actual MC structure.

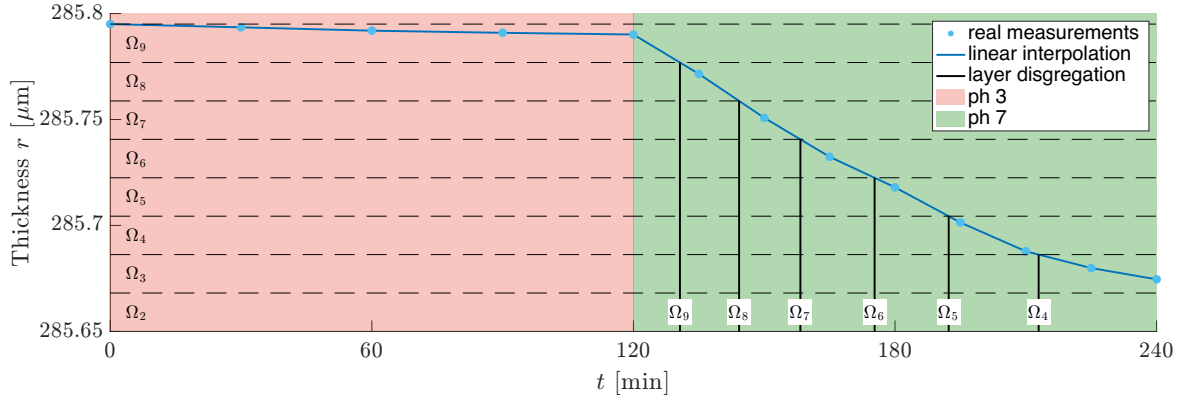

Figure 7. Radius of the eroding MC as a function of time. Radius shrinks due to the erosion of the strata of the shell, which, in turn, depends on the pH during digestive transit.

These results suggest that the encapsulation system provides controlled release, with minimal premature leakage and enhanced delivery in the target intestinal environment.

5.2. Numerical results

The MC model presented in Section 2 contains a number of interdependent parameters, defined within different subdomains, most of which are not known a priori. Moreover, even when estimates of certain parameters are available from the literature, these are often subject to high variability and uncertainty. As a consequence, obtaining reliable estimates is a significant challenge while modeling the release of MCs. Starting from a wide range of physically realistic parameters, we then address this issue in two steps: first, by comparison with experimental data sets, we inversely estimate the parameters for the specific MC release system considered and described in Section 5.1; second, we studied the parameters' sensitivity around the estimated reference values to gain insights on how each component influences the overall release phenomenon.

More in detail, using the experimental values for TA release and the erosion curve from Figure 7, we identify the optimal design parameters $D^+, \alpha, \lambda, \beta$ for each stratum that best fit the experimental dataset. In particular, due to the negligible effect of the oral phase (2 min), we simulated the evolution within gastric (2 h) and intestinal (2 h) phases only, for a total of $T = 14{,}400$ s. The reference parameters we obtained are reported in Table 3.

Table 3. Set of parameters used in the case study. MC's core is divided into 3 strata, only for computational purposes. From top to bottom, the first group of parameters are experimentally measured, the second group are best-fitted parameters matching experimental data, and the third group includes numerical parameters.

Parameter	Core Ω_1 (numerically partitioned)			Shell Ω_2–Ω_9 (8 strata)	
	Ω_1^a	Ω_1^b	Ω_1^c	Ω_2–Ω_3	Ω_4–Ω_9
R [μm]	285.65			285.794	
ΔR [μm]	280	5	0.65	0.0180	0.0180
c_0^{TA} [μg/μm^3]	0			5.085×10^{-3}	2.543×10^{-3}
λ [μm / s]	0.05				
β [s^{-1}]	0				
D^+ [μm^2/s]	6×10^{-7}			5×10^{-6}	10^{-6}
α [dimless]	0.5			0.2	1.0
Δt [s]	1	0.05	0.01		
Δr [μm]	35	0.5	0.005	0.001	

Figure 8 shows the TA concentration profiles up to 240 minutes at time intervals of 10 minutes in the outer part of the core and in the strata of the shell. The initial difference in concentration between pre-coating (Ω_2 and Ω_3) and the other strata progressively smooths out over time, yet allowing a part

of the TA filtrate within the core Ω_1. Upon erosion (cf. progressive vertical drop in concentration), the shell progressively empties, up to when the concentration within the core overcomes the one in the pre-coating; as a consequence, in the later steps of the experiment, the core serves as a reservoir to keep coating concentration high, and allowing a smoother release when paired with a higher outgoing diffusion (cf. Table 3, $\alpha_2, \alpha_3 = 0.2$).

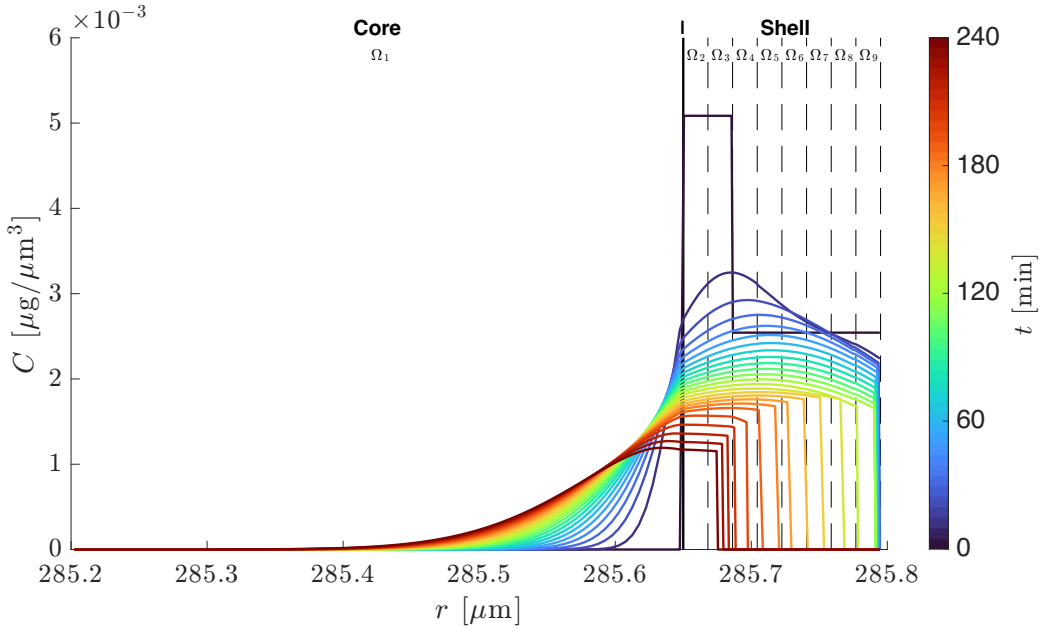

Figure 8. TA concentration profiles at equidistant time intervals (10 min) along the radius on the external part of the MC. Concentration vertical lines correspond to the progressive stratum breakup in consequence of the erosion (cf. vertical lines in Figure 7). The color bar indicates the time scale.

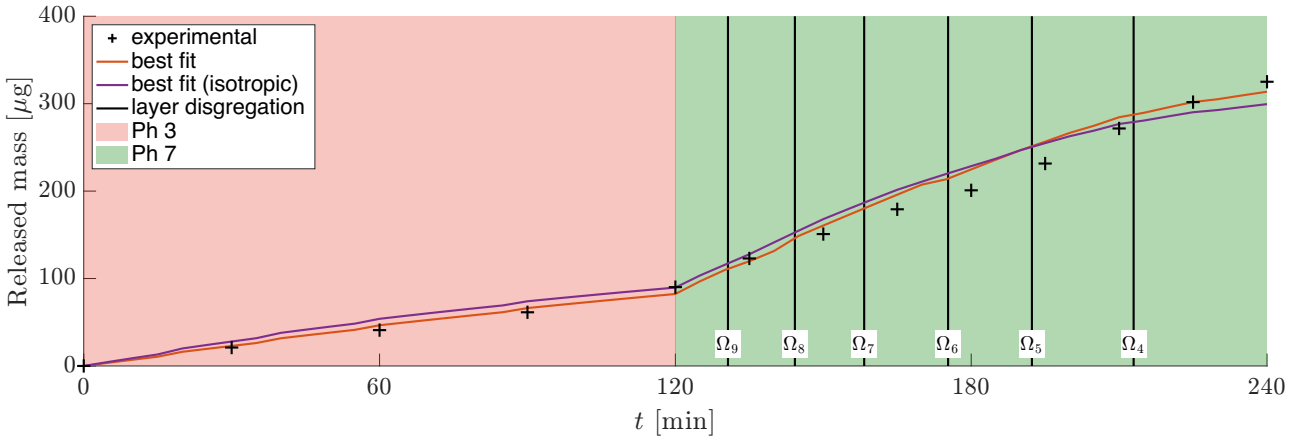

Figure 9. Simulated released TA mass as a function of time, compared with experimental data (crosses). Vertical lines show the stratum breakup time points as a consequence of the erosion. The slope of the profile changes after 120 min, related to faster erosion (cf. Figure 7). Radial asymmetric diffusion provides a better fit in the later points.

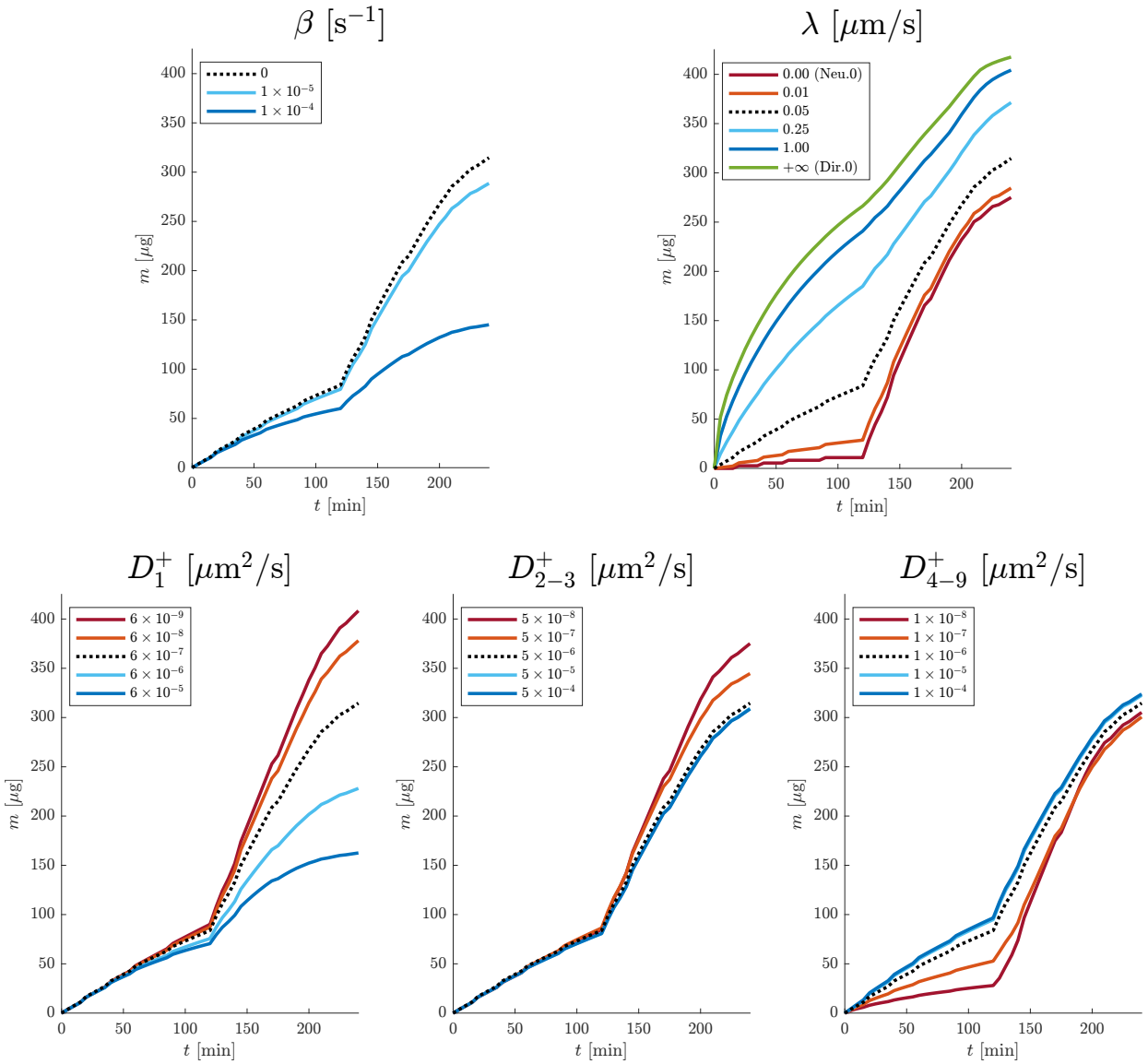

Figure 10. Sensitivity analysis of parameters β, λ, D^+ on the release curves. The dotted black curve refers to the reference values, the other curves refer to larger/smaller values, as in the legends.

In Figure 9, the experimental data are compared with the predictions of the numerical model, with the TA release curve displayed up to 240 minutes. After 120 minutes, the rising of pH (due to the transition from a gastric to intestinal environment) results in a faster release as expected, being yielded by the increase in coating erosion (cf. Figure 8 and Eq 2.15). Particularly interesting is the shape of the release once reaching Ω_3, which remains nearly constant despite a considerable slowing in the erosion process (cf. pre-coating, see also Figure 8). To carefully reproduce this final experimental change, the core must act as a reservoir of TA, as discussed above, actually requiring the diffusion asymmetry of the material for the TA to be released smoothly. In this sense, for completeness, we include the results of the same computational experiment if an isotropic material is considered instead ($\alpha_\ell = 1, \ell = 1, \dots, L$). Here, the overall behavioral difference is negligible, but when the pre-coating is reached, the isotropic

experiment actually slows down the TA release due to progressive emptying of the coating itself.

Parameters' sensitivity The present model depends on a number of parameters bounded to finite ranges to ensure physical compatibility. To understand the relevance of such parameters within the simulation environment, we performed a second set of simulations to analyze the sensitivity of D^+, β, λ, i.e., the parameters most contributing to the overall shape of the releasing curve. In detail, we used the estimation from Section 5.2 as reference values, and we progressively analyzed one parameter at a time to explore the model's different regimes. The sensitivity results are presented in Figure 10, where the details of the implemented variation (order of magnitude for D_ℓ, feasible values for β and λ) are detailed within the plots' legends.

Unsurprisingly, the effect of the retention (binding or decay) parameter β is to reduce the released mass. A larger mass transfer coefficient λ induces a faster release—up to $\lambda = +\infty$ corresponding to a perfect sink—and smooths out the release curve; conversely, its reduction acts as a barrier to the outgoing mass, where $\lambda = 0$ identifies a perfect barrier allowing no TA diffusion, and consequently isolating the erosion contribution to release. Core diffusion coefficient D_1 positively correlates with TA evasion toward the inner part of the capsule, actually leaving less mass to be released due to erosion, particularly visible in the intestinal phase of the experiment (i.e., $t > 120$ min). Analogous is the outcome delivered by the pre-coating diffusion coefficients D_2 and D_3, whose reduction cause less mass to evade toward the core, actually enhancing the release in the intestinal phase; do notice that a value increase does not correspond to a release increase, suggesting a stable point for the dynamic is reached. Finally, conversely to the others, outer coating diffusion coefficients (D_ℓ, $\ell = 4, \dots, 9$) positively correlate with mass release, as expected in regular diffusive processes, allowing for a higher release of mass; their contribution is, however, more limited in the intestinal phase, where erosion leads the release process.

6. Conclusions and future work

Despite significant advances in the development of innovative and smart drug delivery systems, the design and manufacturing of functionalized carriers—particularly those involving multi-stratum architectures—remain open challenges. The release of therapeutic agents from such systems is governed by a complex interplay of chemical, physical, and structural phenomena that are not yet fully understood. In this context, mathematical and computational modeling has become a powerful complementary tool, enabling researchers to probe key mechanisms, reduce the need for extensive experimental testing, and explore diverse scenarios *in silico*.

In this study, we have introduced a mechanistic model to describe drug release from nano-functionalized spherical microcapsules with multi-strata polymer coatings. The model captures coupled diffusive and reactive processes across a multi-scale structure, where micrometric-scale capsules are surrounded by nanometric strata. Modeling transport phenomena across such heterogeneous domains present significant challenges, particularly in handling variable diffusive properties and interfacial coupling.

Grounded in an experimental setup involving a standardized gastrointestinal simulation protocol (INFOGEST 2.0), the proposed model successfully reproduced the observed *in vitro* release profiles. In particular, it captured the releasing effect of the progressive reduction in capsule volume due to

erosion, as well as the distinct release phases. We also found that radial asymmetric diffusion in the early pre-coating strata is essential for correctly describing the dynamics observed during the final release phase, suggesting that microstructural features might affect macroscopic behavior. These findings reinforce the relevance of modeling as a tool to interpret complex datasets and guide formulation choices also demonstrating the importance of tightly integrating modeling and experimentation to extract mechanistic insight and validate predictive capabilities. Concurrently, our computational strategy also facilitates the rational exploration of delivery systems that can meet therapeutic targets with reduced reliance on extensive experimental screening.

In future work, we plan to extend the applicability of the model by including capsule full disintegration and co-delivery of multiple compounds, as well as potentially irregular geometries and heterogeneous coatings with different strata designs. Additionally, simulating patient-specific or pathological gastrointestinal environments (e.g., inflammation, ulcers, or altered enzyme activity) would improve the model translational relevance. Coupling the current framework with pharmacokinetic, pharmacodynamics, immune response models, or co-delivery scenarios might further enhance the model utility for pre-clinical designing and optimization of next-generation drug delivery platforms.

Use of AI tools declaration

The authors declare they have not used Artificial Intelligence (AI) tools in the creation of this article.

Acknowledgements

This work was supported by the NERC Cross–disciplinary Research for Discovery Sciences (NE/X018229/1), the Royal Society International Exchanges 2023 Cost Share Italy (IEC\R2\232063), the Joint Bilateral Agreement CNR (IT) - Royal Society of London (UK) 2024–2025, the Marie Curie programme (HORIZON-MSCA-2024-PF-01-01 n. 101206930-SMartGut Grant), and the ATRAE Talento Consolidado programme (ATR2023-145518) funded by the "Spanish Ministerio de Ciencia, Innovación y Universidades" and the "Agencia Estatal de Investigación".

EO and EC are members of the Gruppo Nazionale Calcolo Scientifico – Istituto Nazionale di Alta Matematica (GNCS–INdAM).

Authors contribution

Conceptualization: EO, EC, JGH, PG, GP. Data curation: JGH, AM, PG. Formal analysis: EO, EC. Funding acquisition: JGH, PG, GP. Investigation – Numerical: EO. Investigation – Experimental: JGH, AM, PG. Methodology – Numerical: EO, EC. Methodology – Experimental: JGH, PG. Resources: JGH, AM, PG. Software: EO. Validation: EO. Visualization: EO. Writing – original draft: EO, EC, JGH, PG, GP. Writing – review and editing: EO, EC, GP. All authors have read and agreed to the published version of the manuscript.

Conflict of interest

Giuseppe Pontrelli is an editorial board member for *Mathematical Biosciences and Engineering* and was not involved in the editorial review or the decision to publish this article. The authors declare there is no conflict of interest.

References

1. R. Bhujel, R. Maharjan, N. A. Kim, S. H. Jeong, Practical quality attributes of polymeric microparticles with current understanding and future perspectives, *J. Drug Delivery Sci. Technol.*, **64** (2021), 102608. http://doi.org/10.1016/j.jddst.2021.102608
2. F. F. Naz, K. U. Shah, Z. R. Niazi, M. Zaman, V. Lim, M. Alfatama, Polymeric microparticles: Synthesis, characterization and *in vitro* evaluation for pulmonary delivery of rifampicin, *Polymers*, **14** (2022), 2491. http://doi.org/10.3390/polym14122491
3. S. E. Birk, A. Boisen, L. H. Nielsen, Polymeric nano- and microparticulate drug delivery systems for treatment of biofilms, *Adv. Drug Delivery Rev.*, **174** (2021), 30–52. http://doi.org/10.1016/j.addr.2021.04.005
4. D. Wei, C. Li, J. Ye, F. Xiang, Y. Xu, J. Liu, Codelivery of survivin inhibitor and chemotherapeutics by tumor-derived microparticles to reverse multidrug resistance in osteosarcoma, *Cell Biol. Int.*, **45** (2021), 382–393. http://doi.org/10.1002/cbin.11494
5. A. Durazzo, A. Nazhand, M. Lucarini, A. G. Atanasov, E. B. Souto, E. Novellino, et al., An updated overview on nanonutraceuticals: Focus on nanoprebiotics and nanoprobiotics, *Int. J. Mol. Sci.*, **21** (2020), 2285. http://doi.org/10.3390/ijms21072285
6. V. Puri, M. Nagpal, I. Singh, M. Singh, G. A. Dhingra, K. Huanbutta, et al., A comprehensive review on nutraceuticals: Therapy support and formulation challenges, *Nutrients*, **14** (2022), 4637. http://doi.org/10.3390/nu14214637
7. E. Lagreca, V. Onesto, C. Di Natale, S. La Manna, P. A. Netti, R. Vecchione, Recent advances in the formulation of PLGA microparticles for controlled drug delivery, *Prog. Biomater.*, **9** (2020), 153–174. http://doi.org/10.1007/s40204-020-00139-y
8. P. Gentile, I. Carmagnola, T. Nardo, V. Chiono, Layer-by-layer assembly for biomedical applications in the last decade, *Nanotechnology*, **26** (2015), 422001. http://doi.org/10.1088/0957-4484/26/42/422001
9. L. Desmond, S. Margini, E. Barchiesi, G. Pontrelli, A. N. Phan, P. Gentile, Layer-by-layer assembly of nanotheranostic particles for simultaneous delivery of docetaxel and doxorubicin to target osteosarcoma, *APL Bioeng.*, **8** (2024), 016113. http://doi.org/10.1063/5.0180831
10. B. Kaoui, M. Lauricella, G. Pontrelli, Mechanistic modelling of drug release from multi-layer capsules, *Comput. Biol. Med.*, **93** (2018), 149–157. http://doi.org/10.1016/j.compbiomed.2017.12.010
11. E. Barchiesi, T. Wareing, L. Desmond, A. N. Phan, P. Gentile, G. Pontrelli, Characterization of the shells in layer-by-layer nanofunctionalized particles: A computational study, *Front. Bioeng. Biotechnol.*, **10** (2022), 888944. http://doi.org/10.3389/fbioe.2022.888944

12. G. Pontrelli, G. Toniolo, S. McGinty, D. Peri, S. Succi, C. Chatgilialoglu, Mathematical modelling of drug delivery from pH-responsive nanocontainers, *Comput. Biol. Med.*, **131** (2021), 104238. http://doi.org/10.1016/j.compbiomed.2021.104238
13. P. Li, M. Müller, M. W. Chang, M. Frettlöh, H. Schönherr, Encapsulation of autoinducer sensing reporter bacteria in reinforced alginate-based microbeads, *ACS Appl. Mater. Interfaces*, **9** (2017), 22321–22331. http://doi.org/10.1021/acsami.7b07166
14. S. Azizi, M. Rezazadeh-Bari, H. Almasi, S. Amiri, Microencapsulation of *Lactobacillus rhamnosus* using sesame protein isolate: Effect of encapsulation method and transglutaminase, *Food Biosci.*, **41** (2021), 101012. http://doi.org/10.1016/j.fbio.2021.101012
15. H. Liu, M. Xie, S. Nie, Recent trends and applications of polysaccharides for microencapsulation of probiotics, *Food Front.*, **1** (2020), 45–59. http://doi.org/10.1002/fft2.11
16. K. Y. Lee, D. J. Mooney, Alginate: Properties and biomedical applications, *Prog. Polym. Sci.*, **37** (2012), 106–126. http://doi.org/10.1016/j.progpolymsci.2011.06.003
17. J. Siepmann, F. Siepmann, Modeling of diffusion controlled drug delivery, *J. Controlled Release*, **161** (2012), 351–362. http://doi.org/10.1016/j.jconrel.2011.10.006
18. J. Crank, *The Mathematics of Diffusion*, Oxford University Press, 1975.
19. L. Xu, V. Kozlovskaya, E. Kharlampieva, J. F. Ankner, S. A. Sukhishvili, Anisotropic diffusion of polyelectrolyte chains within multilayer films, *ACS Macro Lett.*, **1** (2012), 127–130. http://doi.org/10.1021/mz200075x
20. R. J. LeVeque, *Finite Difference Methods for Ordinary and Partial Differential Equations: Steady-state and Time-dependent Problems*, SIAM, 2007.
21. G. Decher, J. Hong, J. Schmitt, Buildup of ultrathin multilayer films by a self-assembly process: Iii. consecutively alternating adsorption of anionic and cationic polyelectrolytes on charged surfaces, *Thin Solid Films*, **210–211** (1992), 831–835. http://doi.org/10.1016/0040-6090(92)90417-A
22. C. Porcel, P. Lavalle, G. Decher, B. Senger, J. C. Voegel, P. Schaaf, Influence of the polyelectrolyte molecular weight on exponentially growing multilayer films in the linear regime, *Langmuir*, **23** (2007), 1898–1904. http://doi.org/10.1021/la062728k
23. A. Brodkorb, L. Egger, M. Alminger, P. Alvito, R. Assunção, S. Ballance, et al., INFOGEST static *in vitro* simulation of gastrointestinal food digestion, *Nat. Protoc.*, **14** (2019), 991–1014. http://doi.org/10.1038/s41596-018-0119-1

AIMS Press